Fuel 262 (2020) 116460

Contents lists available at ScienceDirect

Fuel

journal homepage: www.elsevier.com/locate/fuel

Full Length Article

Flame structure and emission signature in distributed combustion

Rishi Roy, Ashwani K. Gupta*

Mechanical Engineering Department, University of Maryland, College Park, MD 20742, USA

ARTICLE INFO

Keywords:
Colorless distributed combustion
Flame boundary
Flame distribution ratio
Swirl flame structure
Ultra-low pollutants emission

ABSTRACT

Colorless distributed combustion (CDC) combustion technology offers significant advantages of ultra-low pollutants emission, stable operation and improved pattern factor for high intensity stationary gas turbines applications. Detailed knowledge on distributed combustion behavior is required to further deploy this technology. This paper reports the evolution of swirl flame shape, flame expansion and pollutants emission characteristics using propane, methane, and 20% and 40% hydrogen enriched methane fuels. The entrainment of hot reactive gases was simulated by diluting the inlet air stream with inert nitrogen or carbon dioxide. OH* chemiluminescence signatures, captured at different dilution levels, manifested gradual reduction of flame luminosity when CDC was approached. Flame boundaries derived using image threshold technique helped to visualize the broadened reaction zone under CDC conditions, which had much reduced chemiluminescence signal intensity. The rms to mean OH* signal variation at different dilution levels were analyzed to detect the initiation of CDC. The higher flame lift-off observed with CO_2 dilution was due to higher heat capacity of CO_2, resulting in greater flame speed reduction. Flame expansion, evaluated from the area encompassed within the flame boundary at different dilution levels showed a power-law behavior with both the diluents. Expansion of 4 to 5 times of initial flame volumes was observed under CDC using CO_2 and N_2 dilution, respectively. Significant reduction of NO and CO emission achieved under CDC was due to reduction of overall flame temperature, hotspot mitigation, and widened reaction zone occupying large flame volume, which makes it favorable for many practical combustor applications.

1. Introduction

One of the biggest challenges of the 21st century is to harness clean, efficient and sustainable energy production for all propulsion and power generation applications. Unrestrained usage of fossil fuel resources to meet the burgeoning energy demand over the past several decades has resulted in serious concerns on the depletion of conventional energy resources, alarmingly increased global warming, and depletion of the ozone layer that directly impact human health and environment. Increased needs of carbon footprint reduction and stringent regulations by the environmental agencies worldwide for the continued decrease of pollutants emission have led engine manufacturers to focus on new and innovative combustion technologies [1,2]. Besides air pollution and climate control issues, fuel flexibility is another important motivation towards technology innovation in the area of gas turbine research [3]. Of the different available combustion techniques, rich-burn, quick-mix, lean-burn (RQL) [4], lean premixed (LP) [5], flameless oxidation (FLOX) [6,7], moderate or intense low-oxygen dilution (MILD) [8,9], the Colorless Distributed Combustion (CDC) offers good potential for stable combustor operation, nearly zero pollutants emission, noise reduction, fuel flexibility, and superior pattern factor [10–12]. The term 'colorless' is accredited to distributed combustion due to very low visible signatures as compared to the conventional flames. The condition of MILD combustion is achieved when the temperature of the inlet reactant mixture is higher than the self-ignition temperature of the mixture and that the maximum temperature increase with respect to inlet temperature is lower than mixture self-ignition temperature. However, in HiTAC, the inlet temperature is higher than the self-ignition temperature at much lower oxygen concentration that results in relatively small increase in flame temperature during combustion. The CDC technique is governed by the similar fundamental principle of high temperature air combustion (HiTAC) [13]. The HiTAC technology is now widely used in industrial furnaces for significant energy saving and ultra-low emission including noise, and compact size of the equipment. In HiTAC technique, normal air is mixed with the hot gases (via internal or external entrainment) to raise the temperature of fresh reactants above the autoignition temperature before allowing them to mix with fuel. The concentration of O_2 is low in HiTAC so that high temperature of reactants increase only by a small amount depending on the fuel-air mixture strength and air

* Corresponding author.
E-mail address: akgupta@umd.edu (A.K. Gupta).

https://doi.org/10.1016/j.fuel.2019.116460
Received 9 August 2019; Received in revised form 16 October 2019; Accepted 18 October 2019

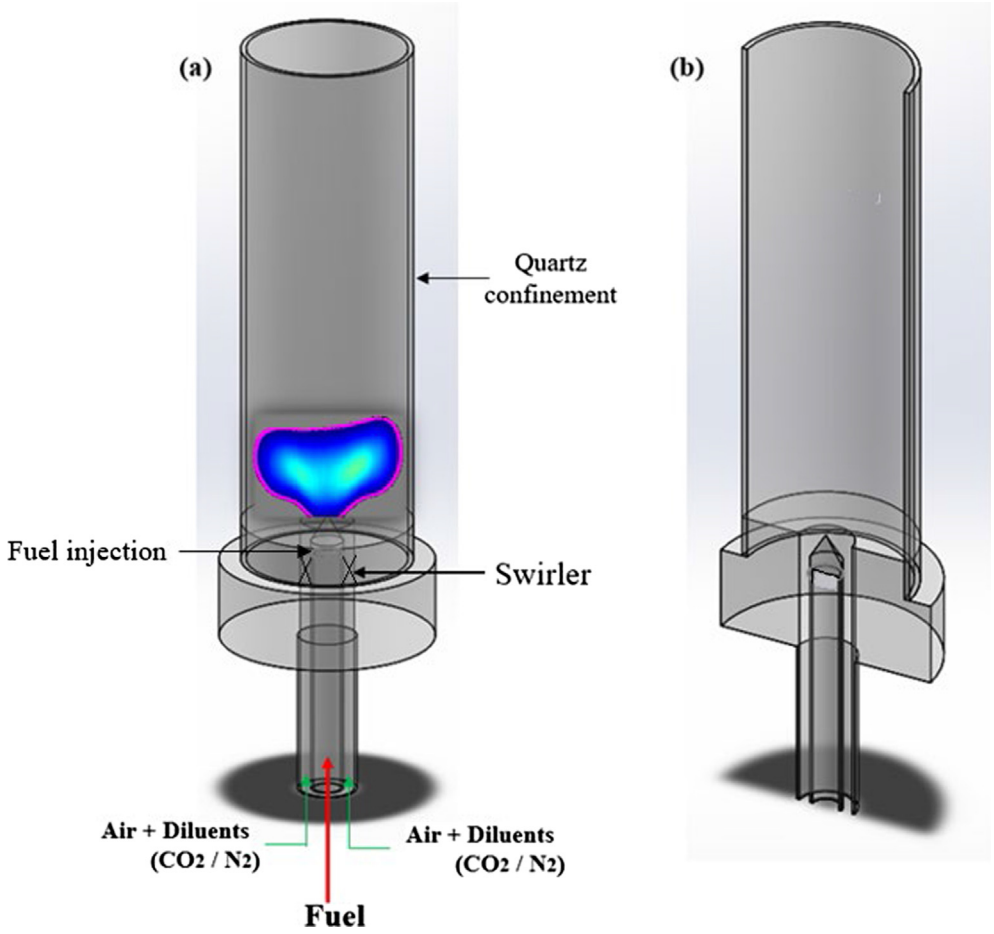

Fig. 1. 3-D representation of (a) swirl burner, and (b) burner cross-sectional view.

preheats. In CDC a uniform mixture of air, fuel and hot reactive gases are reacted at high intensity in a very short residence time (~1 to 3 ms) to avoid the formation of thin reaction zones and hot-spot zones in the flame [14]. The increase in temperature of the reactants and overall reduction in oxygen concentration of the reactive mixture is achieved by internal entrainment of hot combustion products from within the combustor. However, the important criterion is to ensure that the entrainment occurs with a mixing time scale much shorter than the chemical time scale (Damkohler number < 1), so that no chemical reaction initiates before a certain dilution level. In lab scale, such entrainment of reactive gases within the fresh mixture can be simulated by diluting the incoming normal air with inert gases (N_2 or CO_2) [15]. In FLOX, the fuel and air jets are mixed with strongly recirculating combustion products before the onset of chemical reactions. Preheating air is not mandatory in CDC or FLOX combustion. Unlike conventional flames with steep temperature gradient and localized reaction rate and hot-spot zones, the distributed flame possesses a relatively slower reaction rate with flame volume extended over a much larger volume of the combustor. CDC gives rise to a uniform and significantly reduced (in magnitude) temperature field within the combustor. The distributed reaction zone helps to avoid hot-spot formation in flames and mitigate the thermal NO_x generation [16]. These attributes of distributed combustion make it favorable for gas turbine applications.

Different studies have been conducted to understand the physics and chemistry of distributed combustion. Duwig et al. [17] employed laser based diagnostics to image the reaction zone of flameless and distributed turbulent combustion at high resolution. The change of reaction layer structure in relation to distributed (some call it MILD) combustion was investigated by Dally et al. [18]. Pope and Anand [19] made a comparison between the progress variable pdf of distributed and flamelet combustion. A significant contribution has been made by Arghode and Gupta [20–23] towards understanding different aspects of distributed combustion with relevance to gas turbine combustion. Previous studies investigated the effectiveness of distributed combustion for different operating parameters as well as combustor geometries [24,25] for gas turbine applications. In a prior investigation on distributed combustion [26], improved pattern factor along with significant reduction of pollutants emission (NO_x and CO) was reported. Notably, a very high thermal intensity in the range of 156–198 MW/m^3-atm without flame blowout was achieved during this study. Such high thermal intensity signifies the applicability of CDC technology to a wide range of thermal loadings (2–200 MW/m^3). Other technologies such as MILD and FLOX have also shown emission reduction potential at various thermal loading to some extent [27,28]. The effect of flow field configuration was investigated to derive the correlation between the concentrations of pollutants with the given entrainment amounts using particle image velocimetry (PIV) [29]. The initiation of CDC mode in swirl flame was investigated in terms of O_2 concentration in ref. [30]. Several studies were conducted to visualize the global flame shape and OH* chemiluminescence signatures during transition to CDC from a characteristic air-combustion mode [31–33] from a swirl-stabilized burner. However, the extent of the volumetric distribution of flame inside the combustor under CDC mode was not addressed in detail in these studies. The OH* signature reported in the above studies showed a gradual change in flame signature when the flame approached the distributed combustion. Visualization of the exact heat release location was difficult at lower O_2 concentrations due to the very low intensity of OH* signal [34,35]. Such poor visibility was aggravated by the presence of high degree of image noise especially at lower O_2 concentrations (near CDC). Problems of imaging flames with significantly low

OH* signal intensity limit researchers to gain insightful knowledge of the flame shape and location, lift-off distance from the burner exit and the distribution behavior of flames at various flow dilution levels towards CDC. This information is useful to develop a detailed understanding of the distributed combustion process and its suitability for practical combustor design.

This paper presents the flame structure, pollutants emission and spatial location of flames under distributed combustion regime using different gaseous hydrocarbon fuels using a swirl-stabilized combustor. Advanced image filtering technique was employed for noise reduction to derive the flame boundary from the filtered OH* chemiluminescence image. OH* signal intensity variation with O_2 concentrations was examined to detect the initiation of CDC mode. Analysis of the flame area contained within the calculated boundary provided quantification on the extent of flame distribution in the combustor volume at various O_2 levels. The flame lift-off heights were measured to explore the nature of different flames when approaching CDC condition. The NO and CO emissions were evaluated in conjunction with the distributed behavior of flames to provide a better perception of the swirl stabilized distributed flames.

2. Experimental details

A 20 mm inlet diameter, swirl stabilized burner (having 45° swirl angle), fitted to a 200 mm long quartz tube having an internal diameter of 60 mm was used for this study (see Fig. 1). A detailed description of the burner is given in Ref. [36]. Instrument-grade (99.5% pure) propane, chemically pure grade methane and pre-purified H_2 were used to examine flames fueled with propane, methane, 20% and 40% H_2 enriched methane (HEM). Gravimetric flow controllers with an accuracy of 1.5% of full scale were used to meter the fuels and the flow diluent, CO_2. Laminar flow controllers with an accuracy of ± 0.8% of reading ± 0.2% of full scale leading to an overall accuracy of about 1.5% of the reading were used to control the air and the diluent N_2 flow rates. During experimentation, the fuels were injected along the central longitudinal center axis of the swirler in a non-premixed configuration. OH* chemiluminescence images of flames were obtained using an intensified charge-coupled device (ICCD) camera fitted with a narrow band filter, centered at wavelength 307 nm having FWHM (full width at half maximum) of ± 10 nm. The emissions of NO and CO were measured using a gas analyzer having an accuracy of ± 1% of full scale. The NO and CO concentrations were corrected to standard 15% oxygen concentration. The uncertainty in concentrations was estimated to be ± 0.5 PPM for NO, and ± 10% for CO. The reported results were average of three readings for each configuration to assure good repeatability (0.5% of full-scale reading) of data. The reduction of overall O_2 concentrations using inlet flow dilution of air provided the desired conditions of distributed combustion. Table 1 shows the experimental conditions reported here. During the experiments, the heat load, heat release intensity, inlet mixture temperature, and global equivalence ratio (ϕ) of the fuel-oxidizer were held fixed at 3.25 kW, 5.72 MW/m^3-atm and 300 K, and 0.9, respectively. No preheating of air or fuel stream was done prior to their feed into the burner.

Table 1
Experimental conditions.

Gaseous Fuels	Diluent	Air [L/min]	Diluents		Oxygen Concentration [%]
			CO_2 [L/min]	N_2 [L/min]	
Propane (C_3H_8)	CO_2	52.84	0–16.51	0	21–16
	N_2		0	0–26.42	21–14
Methane (CH_4)	CO_2	52.20	0–16.31	0	21–16
	N_2		0	0–26.10	21–14
20% H_2 + 80% CH_4 (20% HEM)	CO_2	51.47	0–16.09	0	21–16
	N_2		0	0–25.74	21–14
40% H_2 + 60% CH_4 (40% HEM)	CO_2	50.23	0–15.70	0	21–16
	N_2		0	0–30.91	21–13

3. Results and discussion

Results on the spatial distribution of heat release rate in flames provide vital information to unravel the different thermal and flow field instabilities, noise as well as pollutants emission during combustion [37–39]. The OH* is one of the most important, spontaneously generated radicals in the chemiluminescence spectrum of any hydrocarbon-air flame which indicates the heat release zone and OH* concentration [40–42]. The location and global structure of the swirl-stabilized flame at different O_2 concentrations corresponding to different flow dilution levels were determined from the OH* chemiluminescence signatures. The derived flame outer boundary was used to evaluate the flame location and distribution inside the combustor during the transition to CDC mode. The primary objective here was to seek further understanding of the distributed nature of different gaseous hydrocarbon flames, obtained from calculating the approximate expansion of the flame boundary (at different O_2 concentration) from the chemiluminescence images. The approach used for the derivation of flame boundary from the OH* chemiluminescence image is given in section 3.1. The evolution of flame shape with N_2 and CO_2 diluents at different concentrations of O_2 (during transition to distributed combustion) is presented in section 3.2. Section 3.3 provides the OH* signal intensity analysis for the detection of CDC mode. The calculation of flame distribution ratio is given in section 3.3 while the pollutants emission characteristics of different fuels is provided in section 3.4.

3.1. Extraction of flame boundary from OH* chemiluminescence image

The flame boundary was calculated from the binarized OH* chemiluminescence image set, generated by using the Otsu thresholding algorithm similar to Sweeney and Hochgreb [43]. The Otsu method is basically an adaptive thresholding technique where the threshold value is decided automatically from the gray-level image histogram analysis. The threshold value is optimized using the discriminant criterion to maximize the separability of the background and foreground pixels [44]. Roy [45] has recently demonstrated a user-defined threshold-based flame boundary detection technique for V-shaped turbulent premixed flames. The resultant OH* chemiluminescence image was filtered with a nonlinear anisotropic diffusion filter [46] modified by the diffusivity model proposed by Perona and Malik [47] for image noise smoothing and edge enhancement. Such image filtering is displayed in Fig. 2 from sample OH* chemiluminescence image of swirling propane flame at two different conditions ($O_2 \sim 21\%$ and 15%). This helps to perceive the noise level and its subsequent reduction (from filtering) under normal air combustion and diluted flow conditions when approaching CDC. Fig. 2a shows the raw and nonlinear filtered OH* chemiluminescence signal of propane-air flame ($O_2 \sim 21\%$) in color map representation (showing an array of red, green and blue intensities). Fig. 2b shows similar images of propane flame at $O_2 \sim 15\%$ in N_2 diluted flow field. The overall quality of the image improved significantly with diffusion filtering. The flame boundary became more defined with the edge smoothing (see the zoomed window in Fig. 2a). The effectiveness of such a noise-filtering technique was further assessed in the context of distributed combustion by measuring the change in image noise levels at different O_2 concentration using the approach of Liu et al. [48]. The corresponding signal to noise ratio (SNR) was also evaluated at different O_2 levels. Fig. 3 represents the noise levels and SNR for the raw and nonlinear filtered chemiluminescence signals at different dilution levels towards distributed combustion. The mean noise level in the raw signal reduced from 39.67 a.u. to 19.35 a.u. using this filter (see Fig. 3a). A remarkable increase of SNR for every O_2 concentration using nonlinear filtering can be observed

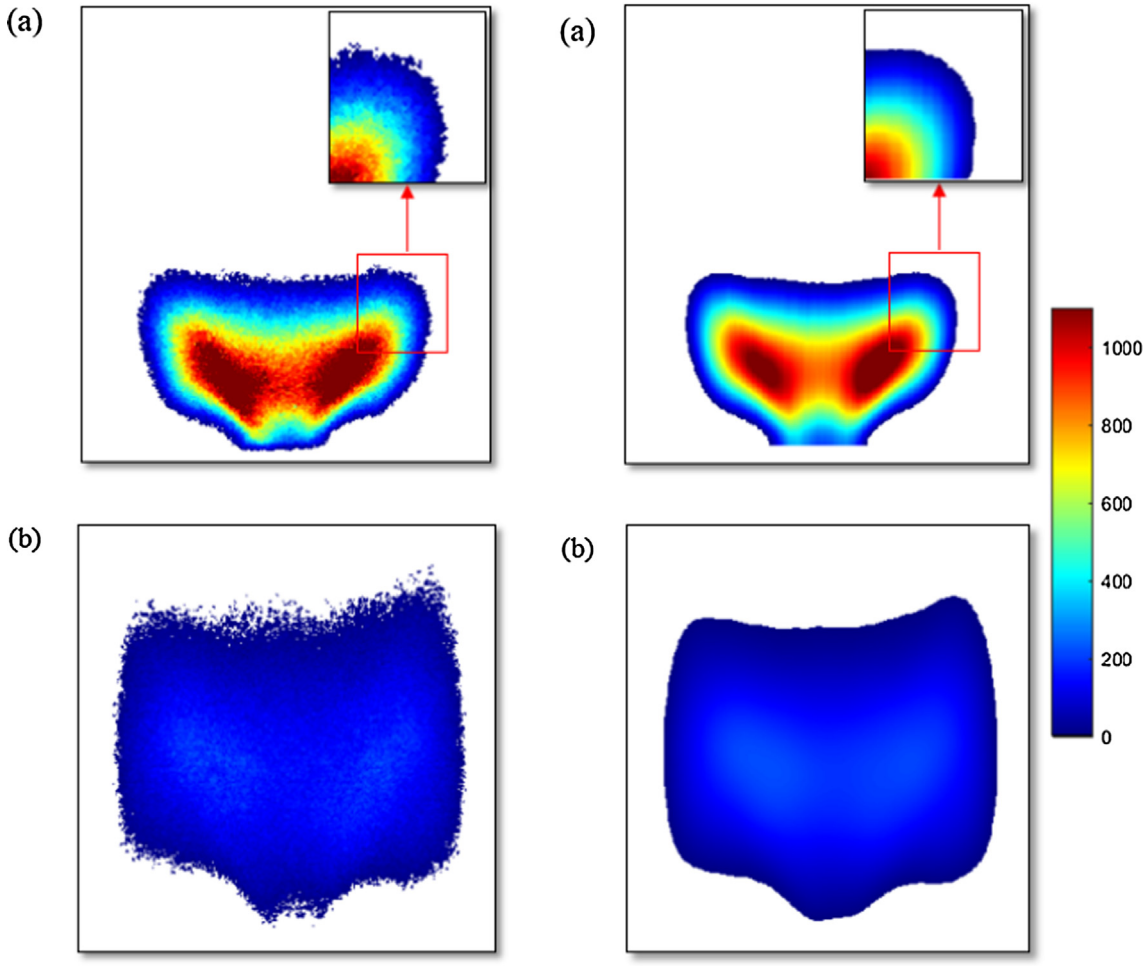

Fig. 2. (a) Unfiltered, raw OH* chemiluminescence signal (left) and nonlinear diffusion filtered signal (right) of propane flame (at $\phi = 0.9$) in air combustion ($O_2 \sim 21\%$). (b) Unfiltered raw OH* chemiluminescence signal (left) and nonlinear diffusion filtered signal (right) of propane flame (at $O_2 \sim 15\%$) using N_2 as the flow diluent (at $\phi = 0.9$).

(see Fig. 3b). The image noise filtering technique is therefore effective for flame visualization in this particular study since the OH* signal level continued to reduce with the decrease in O_2 concentration. The observed trend of decrease in SNR is attributed to gradual reduction of chemiluminescence signals at lower O_2 concentrations. The nonlinear diffusion filtering coupled with Perona and Malik diffusivity model provided effective edge enhancement and image noise reduction for better flame visualization while preserving essential flame features and edges of the actual image. Hence, the results calculated from the derived flame boundary are not influenced by the image filtering.

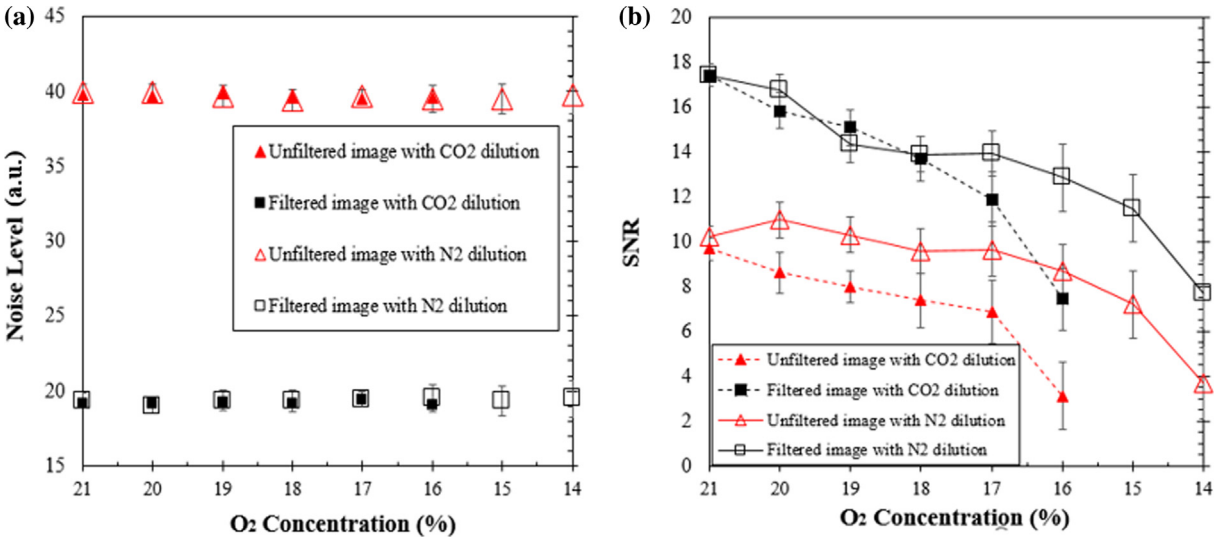

Fig. 3. (a) Noise levels and (b) SNR at different O_2 concentrations of propane flame using CO_2 and N_2 as the inlet flow diluents.

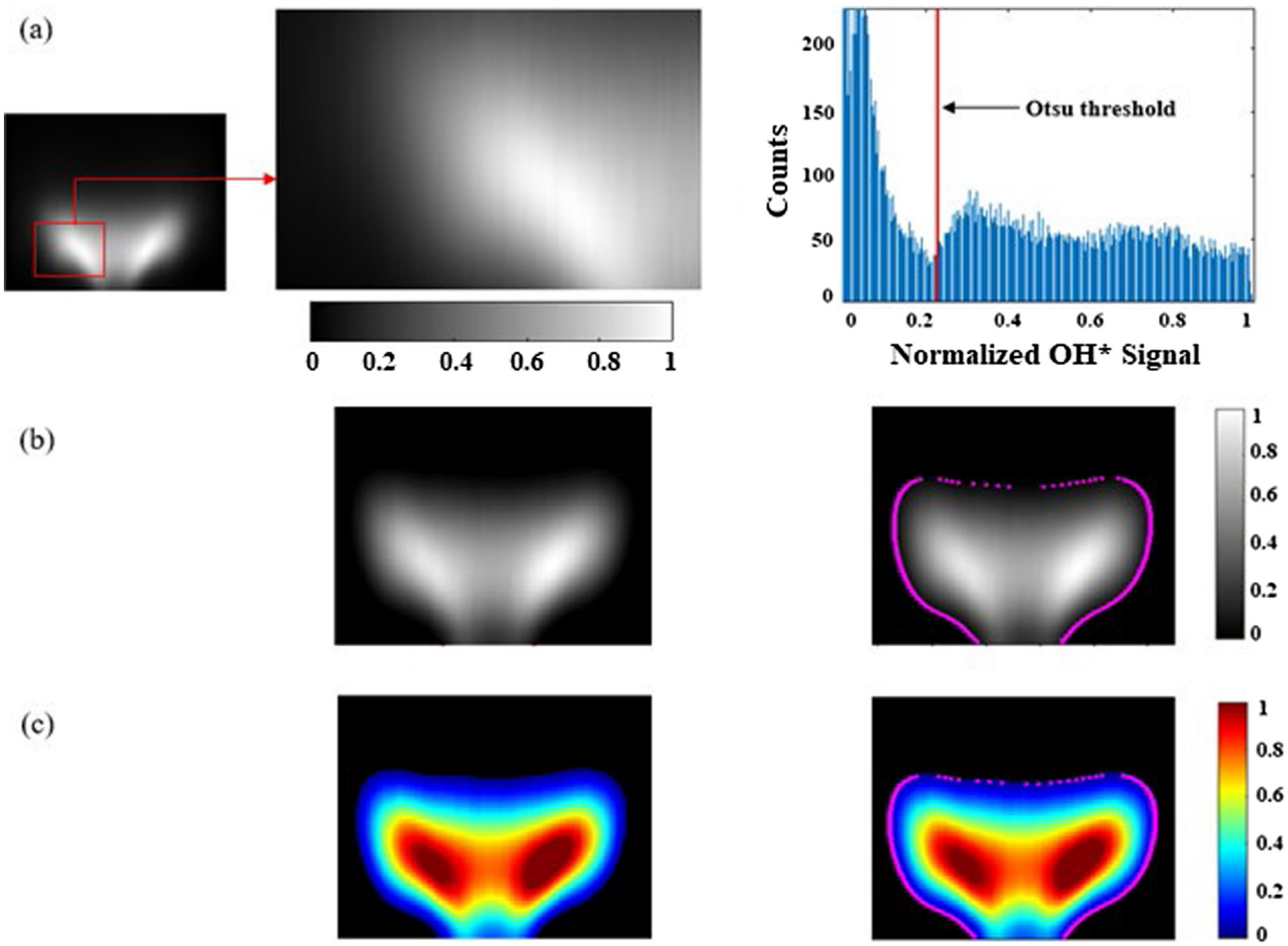

Fig. 4. (a) Otsu threshold (fx1) overlaid on the histogram of filtered propane-air flame ($\phi = 0.9$, $O_2 \sim 21\%$) image. (b) Flame boundary (fx2) overlaid on normalized (black = 0, white = 1) and (c) jet color map signal of OH* chemiluminescence of the similar propane-air flame.

For the OH* boundary detection, the filtered image at each O_2 concentration was converted into a binary map of background (unburned region) and foreground (burnt region) pixels by calculating corresponding 'Otsu' threshold values. The final flame boundary was traced by tracking the intensity jump (from 0 to 1) across the entire span of the binarized image using Matlab© software. The boundary detection process was performed in a specific region near the edge of propane-air flame (at $O_2 \sim 21\%$) (see Fig. 4a) to help assist in histogram analysis for the image pixel counts. The calculated value of the Otsu threshold was verified by locating it on the histogram distribution. The spatial resolution of imaging was measured as 5 pixels/mm. This technique was also verified on the other side of the flame, which showed good compatibility with the former side. The calculated Otsu threshold (represented by the vertical solid line) lies within the first two modes (of the intensity distribution) of the histogram representing the background and flame (OH*) signals, respectively. A reasonable flame boundary can be identified when the threshold value was visually compared in the zoomed flame front (middle image of Fig. 4a). Fig. 4b and 4c represent the calculated flame boundary (magenta outlined) overlaid on the grayscale (normalized between black = 0 and white = 1) and color map appearance for the propane-air flame. A well-defined boundary that precisely matched with the observed contour of OH* emission in both the cases signifies the effectiveness of this technique to examine swirl stabilized flames. We used this approach to extract the flame boundary at different O_2 concentration. The sensitivity analysis of the flame edge location with respect to the image binarization threshold showed an approximate flame area change of 4% for every 10% offset of binarization threshold from the calculated Otsu threshold value. Some apparent discontinuity of the flame boundary near to the uppermost part of the flame is attributed to the presence of nearly flat flame at that region, for which the computational code was unable to find the above-stated intensity jump (0–1) and that contributed to discontinuity in that region.

3.2. *Flame structure evolution while approaching distributed combustion regime*

The spatial and structural evolution of different gaseous hydrocarbon flames along with their distributed behavior in the swirl combustor was investigated using the flame boundary approach. Flame shapes at different O_2 concentrations were examined using propane, methane, and hydrogen enriched methane-oxidizer compositions. Fig. 5 shows different flame shapes using normal air (at $O_2 \sim 21\%$) without any diluent. The spatial distribution of OH* chemiluminescence intensity is presented in a color bar with a scale of 0–1000 a.u. The results depict the expected luminosity of propane-air swirl flame to be higher than the corresponding methane or hydrogen-enriched methane flames. Higher energy release per unit volume of propane-air flame than the methane-air flames [49] provided high OH* chemiluminescence signal intensity (strongest at the center), see Fig. 5 (a) and (b). Hydrogen enriched methane flames showed a gradual decrease in flame length, as compared to propane and methane flames. This is attributed to enhanced reactivity and higher flame speed of the combustible mixture associated with the increase in hydrogen content to methane. Similar

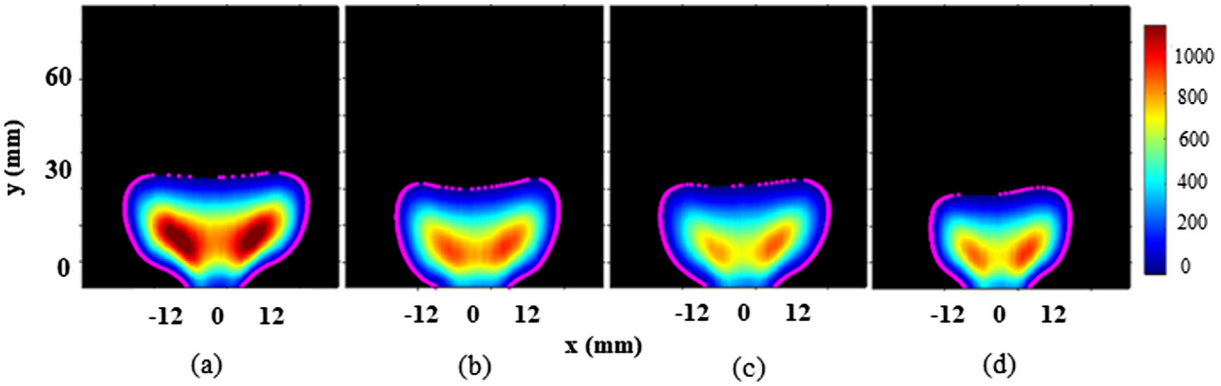

Fig. 5. Representation of undiluted (a) propane (b) methane (c) 20% HEM, and (d) 40% HEM flames using normal air as the oxidizer (at $O_2 \sim 21\%$).

Table 2
Calculated flame area of different flames using normal air as oxidizer.

Fuel-air	Propane-air	Methane-air	20% HEM	40% HEM
Area (mm^2)	1034.91 ± 10	895 ± 7	888 ± 5	712 ± 5

observations of reduced flame length were reported in the previous studies [50,51] of hydrogen enriched methane swirl flames. To further understand the flame shape and size, the two-dimensional flame area was evaluated from the chemiluminescence images of different fuel mixtures under normal air-combustion condition ($O_2 \sim 21\%$). The results are shown in Table 2. The results on flame area shown in Table 2 manifest that the burning area (or volume in three dimensions) for the propane-air composition is highest among all the different hydrocarbon flames reported here.

The gradual transition of flames to CDC mode was examined using OH* chemiluminescence imaging at different flow dilution levels (using CO_2 or N_2). Fig. 6 exhibits the shape and relative location of the different flame boundaries for each O_2 concentrations using CO_2 as the diluent. The decrease in O_2 concentrations provided a gradual broadening of the flame area. Such widening of the flame is accompanied with a gradual decay of the concentrated OH* zone (red) near the central part of the flame (see Fig. 6a, at $O_2 \sim 21\%$) to a uniformly distributed low intensity signal extended over the entire flame volume (see last column of flames in Fig. 6). This indicates that the flame gradually approached the distributed combustion regime. Similar observations on flame widening and near colorless swirl flame in distributed combustion were reported in ref. [52]. The reduction in spatial concentration gradient of OH* with the decrease in O_2 level in the fresh mixture signifies a gradual reduction of reaction rate per unit flame volume to increase the net burning volume of the flame. The similarity in the evolutionary pattern of different hydrocarbon flames is observed in Fig. 6; however, the O_2 concentration at which the OH* signal distribution began to change to an overall uniform intensity distribution, varied with the fuel composition. A nearly uniform OH* signal distribution for propane flame occurred at $O_2 \sim 17\%$, whereas it occurred at 18% for methane flame. The flame images at $O_2 = 16\%$, correspond to final unextinguished state in the reactive flow field. Global flame extinctions were observed at $O_2 < 16\%$ with a slight change in blow-off equivalence ratios (ϕ_{bo}) among the fuel-oxidizers examined. The ϕ_{bo} for propane flame was observed to be higher than methane and HEM flames. The reduction of reaction rate due to the addition of diluent caused decrease in flame speed and hence, the flame lifts off from the burner exit plane. Lift-off caused the shape of the flame base to gradually change from point shaped flame to a nearly flat shape. For the propane and methane flames, the pointed base was observed up to $O_2 = 16\%$, which is attributed to near blow-off flame quenching. A similar flame evolution was demonstrated in Fig. 7, using N_2 as the diluent gas. Gradual flame broadening with a decrease in visible flame signature, flame lift-off with flow dilution (or decreasing O_2 concentration) are consistent with the previous observations made using CO_2 as the diluent gas. The flame blow-off limits extended with N_2 dilution (see Fig. 7). The stable flame was observed until $O_2 = 14\%$ (while it was 13% for 40% HEM fuel) unlike CO_2 dilution case where the flame sustained only up to $O_2 = 16\%$. This was conjectured to higher heat capacity value of CO_2 as compared to N_2 [53], which provided a greater reduction of flame speed as well as the overall temperature [54] at a relatively higher O_2 concentration. Hence, the N_2 diluted flow field provides stable flames over an extended range of O_2 concentration due to its delayed transition to CDC mode as compared to the CO_2 dilution case.

The flame lift-off heights (h) at different O_2 concentration using the two different diluents are presented to help understand the stability and reactivity of swirl-stabilized flames. The normalized lift-off heights (with respect to the burner exit diameter, D) were evaluated from the distance between the burner exit and the flame base (mean altitude value of the base) as marked by the derived flame boundary for each flow condition. The results are represented in Fig. 8. The results show that below a certain threshold value of O_2 concentration (~20% for CO_2 and 19% for N_2 diluted cases) all flames exhibited some lift-off from the burner exit. The lift-off heights for the CO_2 diluted flow field are higher than the N_2 diluted flow field. As mentioned earlier, the higher heat capacity of CO_2 provided greater reduction of flame speed and subsequently, higher flame lift-off heights than the N_2 dilution case were observed. The methane flame revealed the highest lift-off value for both the diluents. This was conjectured to be associated with the reduction of mixture reactivity, which was highest for methane as compared to other fuels for every O_2 concentrations reported here. The reduction in flame speed for methane mixture was highest among the fuels that resulted in the largest flame lift-off distance for all O_2 concentrations examined. Hydrogen enriched methane flames showed less flame lift-off height than pure methane flame. This is directly attributed to increased reactivity and the flame speed due to the addition of H_2 with methane, which helped to stabilize the flame close to the burner exit.

3.3. OH* signal intensity based CDC mode detection

Chemiluminescence signal intensity variation at different O_2 concentrations was analyzed to detect the initiation of CDC. The ratio of rms to mean OH* signal intensity (I_{rms}/I_m) was measured for every O_2 level and presented in Fig. 9. Propane flame images are overlaid on the plot to compare the spatial intensity variation corresponding to different O_2 levels. The highest intensity fluctuation (rms = 20–25% of mean intensity) is observed in air combustion conditions ($O_2 \sim 21\%$) for different flames. Propane flames have the highest I_{rms}/I_m values, signifying a relatively higher spatial OH* intensity variation than other flames. The value of I_{rms}/I_m gradually decreased with decrease in O_2

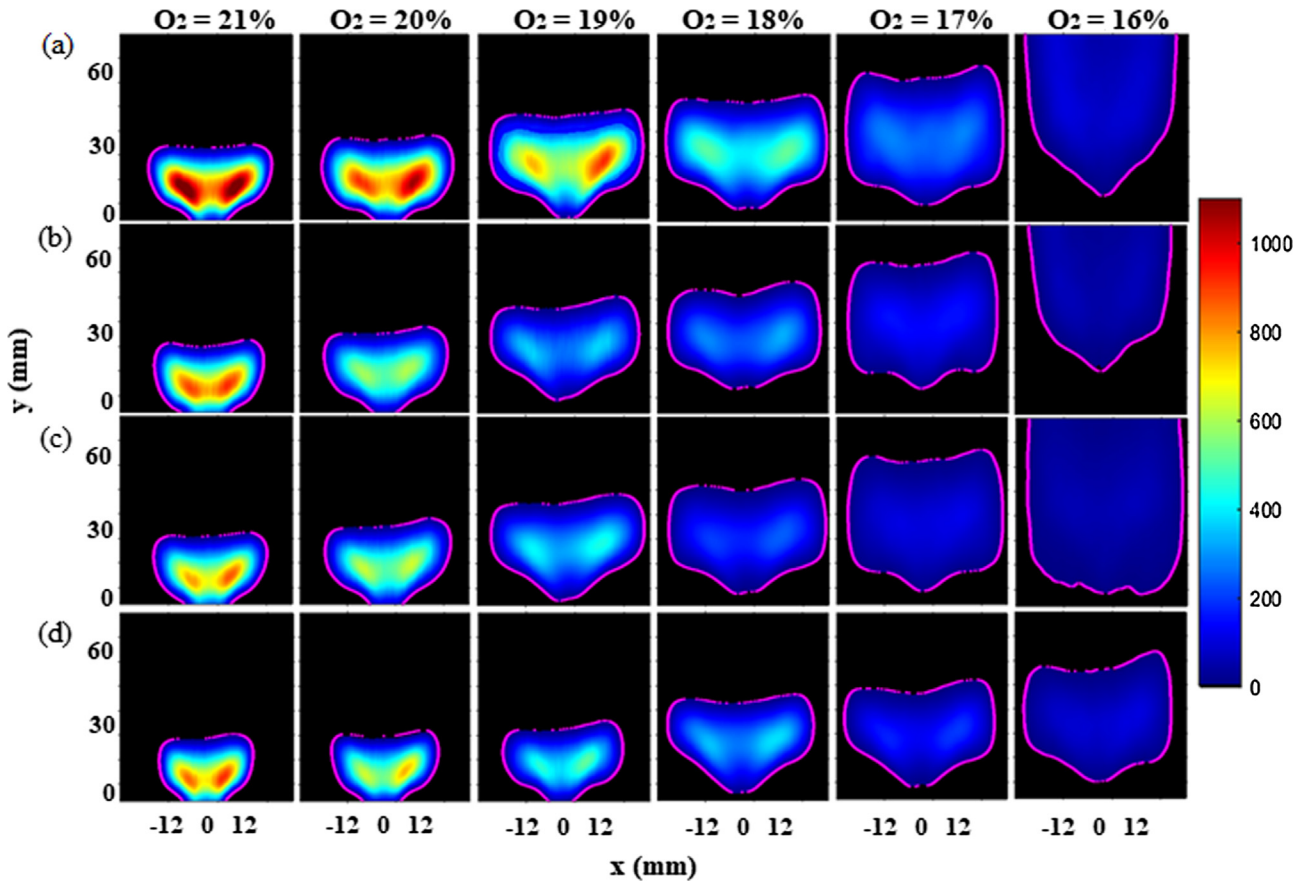

Fig. 6. OH* chemiluminescence with overlaid flame boundary for (a) propane, (b) methane (c) 20% HEM, and (d) 40% HEM flames at different O_2 concentrations using CO_2 as diluent.

concentration of the fresh reactant mixture for both CO_2 and N_2 diluted flow cases. Such reduction in rms intensity fluctuation was expected from the gradually diminishing spatial gradient of OH* distribution to form uniform spatial distribution approaching CDC (see Figs. 6 and 7). The slope of the I_{rms}/I_m curves gradually changed to zero at $O_2 \leq 17\%$ and 15% for CO_2 and N_2 dilution cases, respectively. The corresponding rms intensity values of different flames were found to become less than 2% of their mean intensity. This indicated an almost negligible spatial variation of OH* signal in flames below the above given O_2 levels. The uniformity of OH* concentration gradient in CDC is confirmed from the overlaid propane flame images. The results infer that distributed combustion starts at $O_2 \sim 17\%$ and 15% for CO_2 and N_2 diluted flow fields and exists until the flame blow-off.

3.4. Calculation of distribution ratio

A quantitative analysis of the OH* chemiluminescence image help assists to understand the distribution behavior of flames in a swirl burner. Distribution Ratio (DR) is defined as the ratio of the observed flame area (A_f) from the chemiluminescence image at any particular O_2 concentration to the initial flame area (A_i) at normal air condition, $O_2 \sim 21\%$, so that:

$$\text{Distribution ratio, } DR = \frac{A_f}{A_i} \quad (1)$$

The magnitude of A_f was obtained by measuring the area within the flame boundary derived from the chemiluminescence image. The A_i values are given in Table 2. The concept DR is important to understand the distributed behavior of different swirl flames at the transition to CDC. Simultaneous examination of DR and OH* intensity fluctuation (I_{rms}/I_m) is useful to detect the CDC regime in terms of flame expansion.

Fig. 10 shows the variation of DR and I_{rms}/I_m with different O_2 concentrations for CO_2 and N_2 diluted flow field. A gradual increase in DR value was observed with a decrease in O_2 concentrations for both diluent gases. The results show the following power-law behavior of flame expansion for both CO_2 and N_2 diluted flow fields:

$$DR_{CO2} = 445762 * [O_2]^{-4.273}; \ R^2 = 0.9998 \quad (2)$$

and

$$DR_{N2} = 9414.4 * [O_2]^{-3.021}; \ R^2 = 0.9960 \quad (3)$$

At the initiation of CDC mode determined from the OH* signal intensity analysis (in section 3.3), the DR possesses a value of ~2.5 for all the flames. This signifies that flames undergo an expansion of at least 2.5 times of their initial volumes (in normal air combustion) before transitioning to CDC. The different combustion modes for these flames can be expressed by the following DR values:

$$DR = 1 \, for \, air \, combustion \, (O_2 \sim 21\%)$$
$$DR \geqslant 2.5 \, for \, distributed \, combustion$$

The final values of DR showed a significant volumetric expansion of flames under distributed combustion conditions. Expansion of nearly three times of the initial volumes (in air combustion) was found for different flames using CO_2 as diluent while it was more than 3.5 for the N_2 dilution case. Approximate flame distribution can be measured using the above-stated DR models for different diluents. The DR values are more sensitive to the flame edge location at lower O_2 concentration. In CDC mode, an average change of 10.5% of DR value for every 20% offset of the threshold value (from Otsu threshold) was noted from the sensitivity analysis.

The above calculation of distribution ratio, DR is based on 2D flame areas. Flame areas were obtained by imaging the flame in its mid-plane.

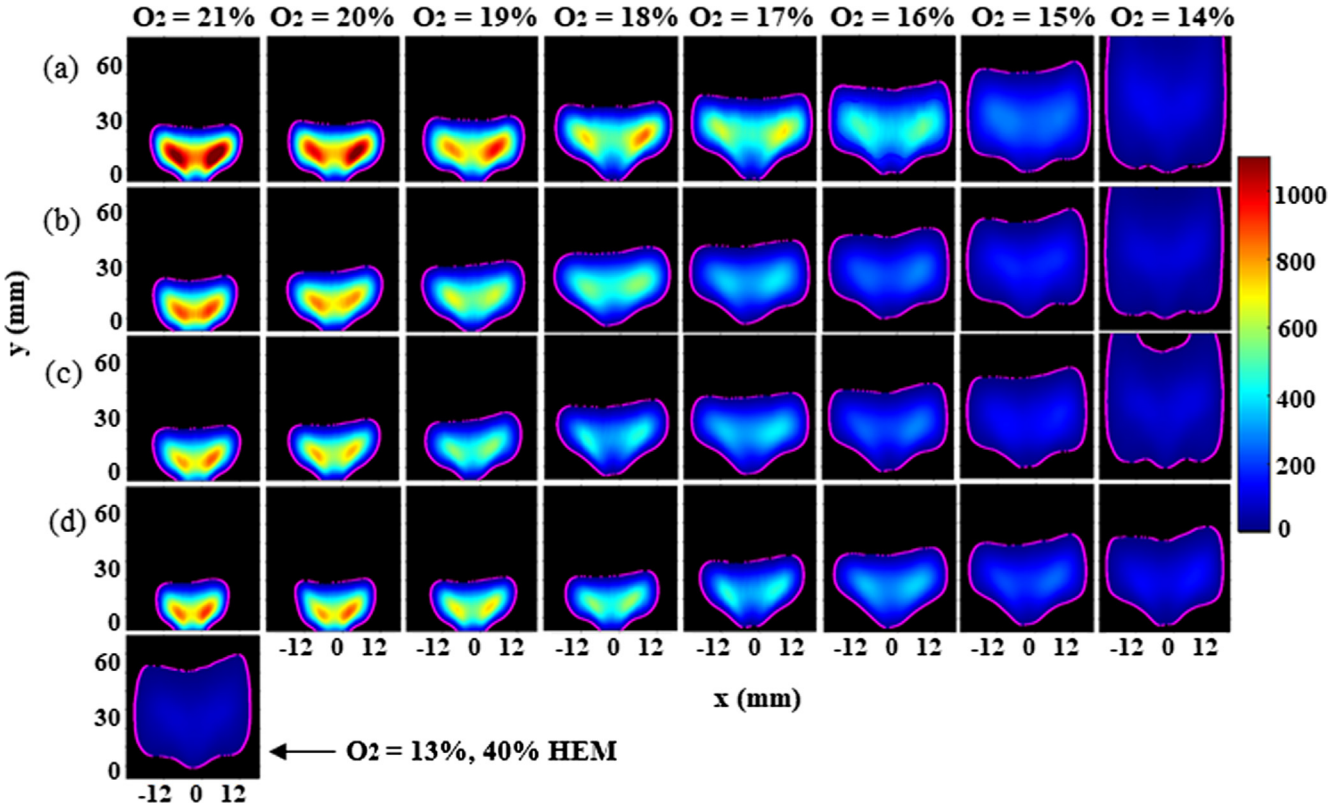

Fig. 7. OH* chemiluminescence with overlaid flame boundary for (a) propane, (b) methane (c) 20% HEM, and (d) 40% HEM flames at different O_2 concentrations using N_2 as diluent.

It may not always provide a true measure of the volumetric distribution of flames. We also calculated the actual volume of the flames by solid revolution of 2D images in Matlab® to calculate a volume-based distribution ratio, DR. A multiplication factor (M_c) to convert the mean DR (area) values to mean DR (volume) was calculated, such that:

$$\text{DR (volume)} = M_c * \text{DR (area)} \quad (4)$$

The DR (volume) and the M_c values are reported in Table 3 along with the DR (area) values for different flow dilution cases. The volume-based DR from Table 3 manifests that the flame expands more than 4 times (for CO_2) and nearly 5 times (for N_2) of their initial volumes under CDC mode.

Note that DR may vary with swirl distribution in the burner. The DR values of methane and 20% HEM flames in CDC are higher than the propane flame. This is due to relatively lower A_i values and comparable sizes of these flames to those of propane flame under CDC. The 40% HEM flame showed a slightly different expansion nature (especially with N_2 dilution) due to its significantly smaller flame shape (A_f) at every O_2 level. Such smaller shape is from the result of high mixture reactivity and flame speed due to higher H_2 content in the mixture. Stable OH* chemiluminescence image for 40% HEM mixture was recorded with up to O_2 = 13% as compared to 14% for other fuel-oxidizer mixtures examined using N_2 dilution. Such extension of flammability limit can be explained using the concept of DR and corresponding lift-off information shown in Fig. 8. The lifted flame is more unstable than an attached flame and the degree of instability increases with an

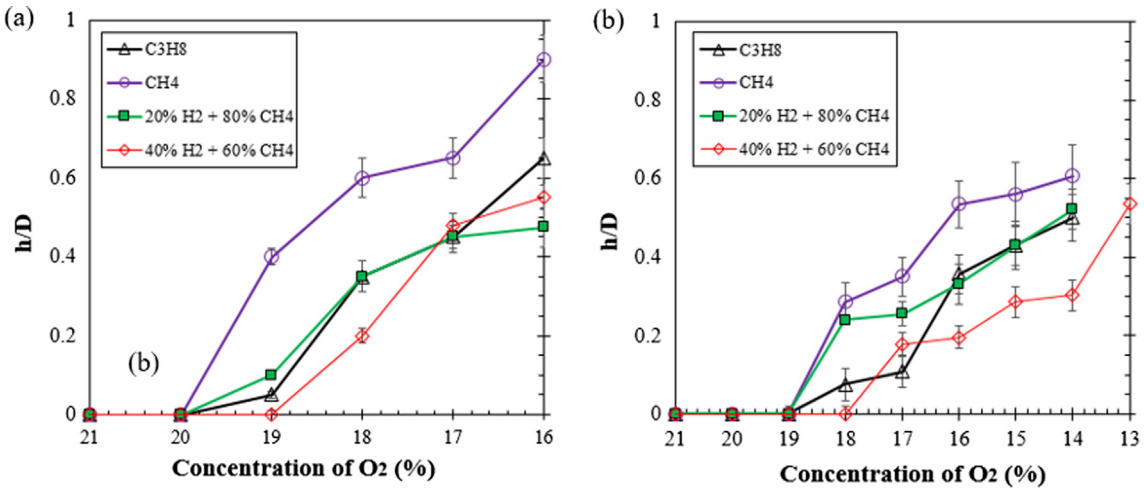

Fig. 8. Normalized lift-off heights for different fuel-oxidizer flames at different O_2 concentrations with (a) CO_2, and (b) N_2 as inlet flow diluent.

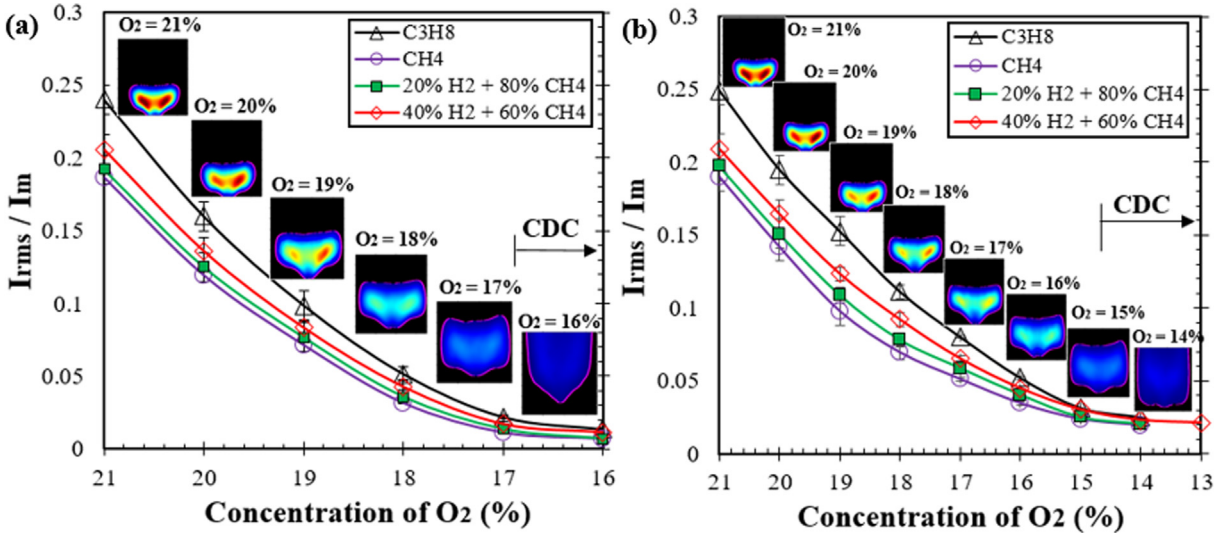

Fig. 9. RMS to mean OH* signal intensity (Irms/Im) variation with O_2 concentrations for different flames with (a) CO_2, and (b) N_2 as inlet flow diluent. (Propane flames are overlaid).

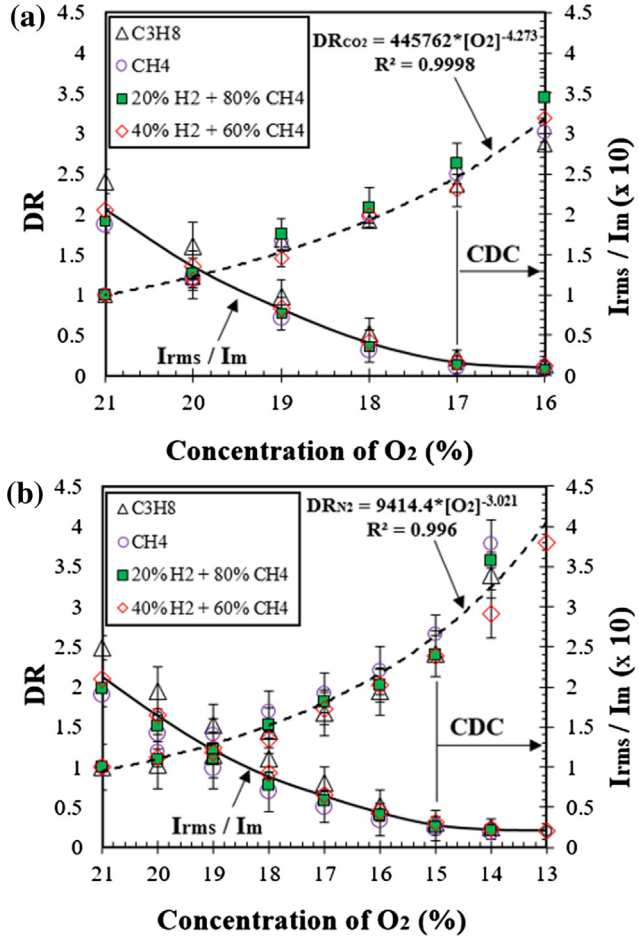

Fig. 10. Distribution Ratio (area-based) for different hydrocarbon flames at different O_2 concentrations using (a) CO_2 and (b) N_2 as the diluent.

increase in lift-off heights [55]. The normalized lift-off height for 40% HEM with N_2 (see Fig. 8b) dilution is seen to be lower than other flames under consideration. At O_2 = 14%, the lift-off distance of this flame was less than 50% of the other hydrocarbon flames. This revealed that the flame stabilized relatively close to the burner exit. The lowest magnitude of DR (at O_2 = 14%) among different hydrocarbon flames describes a relatively narrow shape of this flame due to energetic and stable burning characteristics. Such stable burning behavior even at O_2 = 14% helps this particular flame to sustain for longer time.

3.5. NO and CO emission

The emission of NO and CO under normal air combustion and distributed combustion were obtained. The concentrations of NO and CO corrected to 15% O_2 concentration (ppm) under air combustion (at $O_2 \sim 21\%$) are given in Table 4. The flame temperature has a pronounced effect on NO_x formation [56]. The NO emission from methane-air flame is seen to be lower than the propane-air flame which has a higher flame temperature. The concentration of NO gradually increased with an increase in hydrogen enrichment to methane. In Ref. [51], this increase of NO was attributed to the increase in local flame temperature from hydrogen addition as well as broadening of post combustion zone. The formation of NO and CO was examined in relation to DR at each O_2 concentration to understand the pollutants emission when approaching CDC. The NO and CO concentrations were normalized with respect to their initial concentrations (given in Table 4) and expressed as NO* and CO*. Fig. 11 shows the NO*, CO*, and DR at different O_2 levels using CO_2 as the flow diluent. The variation of DR, NO* and CO* helps to understand the effectiveness of combustion at different O_2 levels. The NO* decreased for every fuel with an increase in flow dilution when approaching towards distributed combustion regime. An average reduction of 90% (96% for propane and 40% HEM flames) of the initial NO concentration (under normal air combustion mode) was observed when the flame transitions to CDC. The gradual reduction of NO level is related to the drop in overall adiabatic flame temperature with increasing flow dilution as found in our previous studies [32,35]. The adiabatic flame temperatures at various flow dilution level was supported by performing simulation in Chemkin-Pro® coupled with GRI-3.0 [57] for different hydrocarbon flames considered here. The results on the adiabatic flame temperature of these fuels are shown in Fig. 12 for both the diluents. As expected the adiabatic flame temperature gradually decreased with increase in flow dilution for both the diluents. The rate of temperature decrease was higher for the CO_2 diluted flames (than N_2 diluted flames) due to the higher heat capacity value of CO_2 resulting in greater reduction of temperature with flow dilution. In addition to NO*, the CO* levels were also reduced to about half of their initial values, when flames transitioned to CDC. This is attributed to the gradual reduction of varying stoichiometry and sharp temperature gradient (that exist in conventional fuel-air flames) with decrease in O_2

Table 3
DR (volume) and Multiplication factor (M_c) at different flow dilution levels.

O_2 (%)	CO_2 dilution case			N_2 dilution case		
	DR (area)	DR (Volume)	Multiplication factor (M_c)	DR (area)	DR (Volume)	Multiplication factor (M_c)
21	1	1	1	1	1	1
20	1.228	1.430415	1.164833	1.109152	1.296279	1.168712
19	1.47	2.058124	1.400085	1.27	1.523972	1.199978
18	1.94	2.673674	1.378182	1.48849	1.999213	1.343114
17	2.48	3.501241	1.411791	1.770545	2.434335	1.374907
16	3.12	4.145295	1.32862	2.11	3.096282	1.467432
15	–	–	–	2.55	3.713924	1.456441
14	–	–	–	3.41	4.861688	1.425715
13	–	–	–	4.12	4.880121	1.184495

Table 4
NO and CO (corrected to 15% O_2) concentrations in normal air-combustion.

Fuel-air	Propane-air	Methane-air	20% HEM	40% HEM
NO (ppm)	20.29	13.23	13.44	13.93
CO (ppm)	56.44	52.12	24.6	28.64

level. Subsequently, improved mixing and uniformity in combustion are fostered across the combustor volume [33] which results in reduction of CO*. Note that CO* suddenly increased at some intermediate O_2 levels. This is primarily attributed to the dissociation of CO_2 to CO at high temperature. Such sudden rise in CO level was further investigated using simplified chemical analysis of the present flame. The analysis was performed in Chemkin-Pro (with GRI 3.0) for a sample case of 20% hydrogen enriched methane where such rise (in CO level) was prominent. A similar trend of high CO level at intermediate O_2 level was demonstrated by the Chemkin simulation. Analysis of reaction pathways revealed the presence of a particular reaction step: $CH_2(s) + CO_2 \leftrightarrow CO + CH_2O$ for the diluted flow cases. Here the $CH_2(s)$ represents singlet methylene [58]. This specific reaction step was absent in normal combustion mode with pure air as the oxidizer. Additionally, this reaction step was gradually prioritized with increase in flow dilution

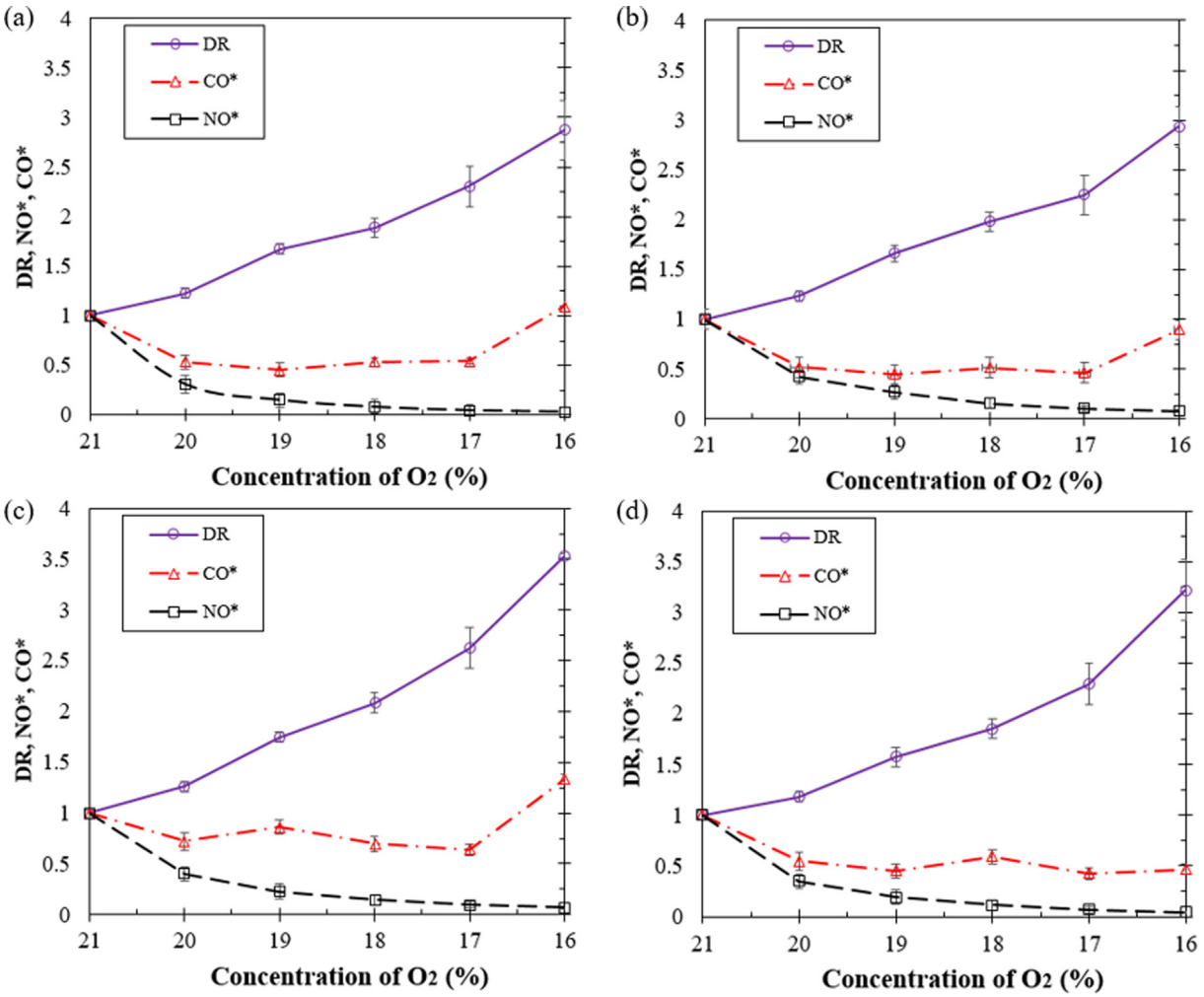

Fig. 11. Normalized NO (or NO*) and CO (or CO*) and DR (area-based) for (a) propane, (b) methane, (c) 20% HEM and (d) 40% HEM flame at different O_2 concentrations using CO_2 as flow diluent.

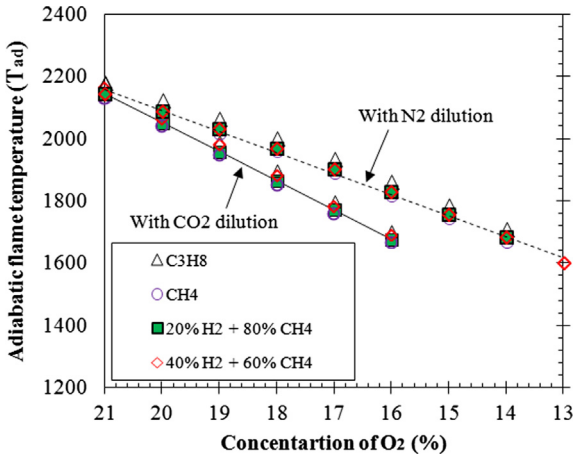

Fig. 12. Adiabatic flame temperature of different hydrocarbon flames at various O_2 concentrations with CO_2 and N_2 as flow diluents.

levels. For the O_2 concentrations corresponding to the sudden rise of CO, the direction of the above-stated reaction was found to be in the forward direction that favored the CO formation. The same reaction step was also reported by Leung and Lindstedt [59] for CO formation. Such observation suitably supports the role of this particular reaction step in enhanced CO production.

The effect of flow dilution with N_2 on NO and CO emission was also examined. Fig. 13 shows the NO* and CO* emission behavior at different O_2 concentrations with N_2 dilution. The observation commensurate with the CO_2 diluted flow field case. The decrease in the O_2 level decreased the NO* and CO* while increasing the DR. The additional CO production from the dissociation of CO_2 at intermediate O_2 levels was absent in N_2 dilution case. A comparison of Figs. 11 and 13 show that larger flame distribution inside the combustor as well as extended flammability limit with ultra-low NO and CO emission can be achieved using N_2 as flow diluent.

4. Conclusions

An experimental investigation on distributed combustion in a swirl burner was carried out using four different gaseous fuels, namely, propane, methane, 20% hydrogen enriched (80% methane) and 40% hydrogen enriched (60% methane) methane. The primary motivation of this study was to understand the global flame behavior and pollutant emission in distributed combustion. Flames were recorded by imaging the OH* chemiluminescence signatures. Nonlinear diffusion filtering was employed for noise smoothing and flame edge enhancements of the chemiluminescence images. The flame boundary was extracted from the binarized version of the filtered chemiluminescence images by applying the Otsu thresholding algorithm. Resulting flame images were examined at different O_2 concentrations (corresponding to different dilution levels) when approaching distributed combustion condition. Analysis of OH* signal intensity variation with O_2 concentrations helped to detect the onset of CDC mode. The rms OH* signal intensity

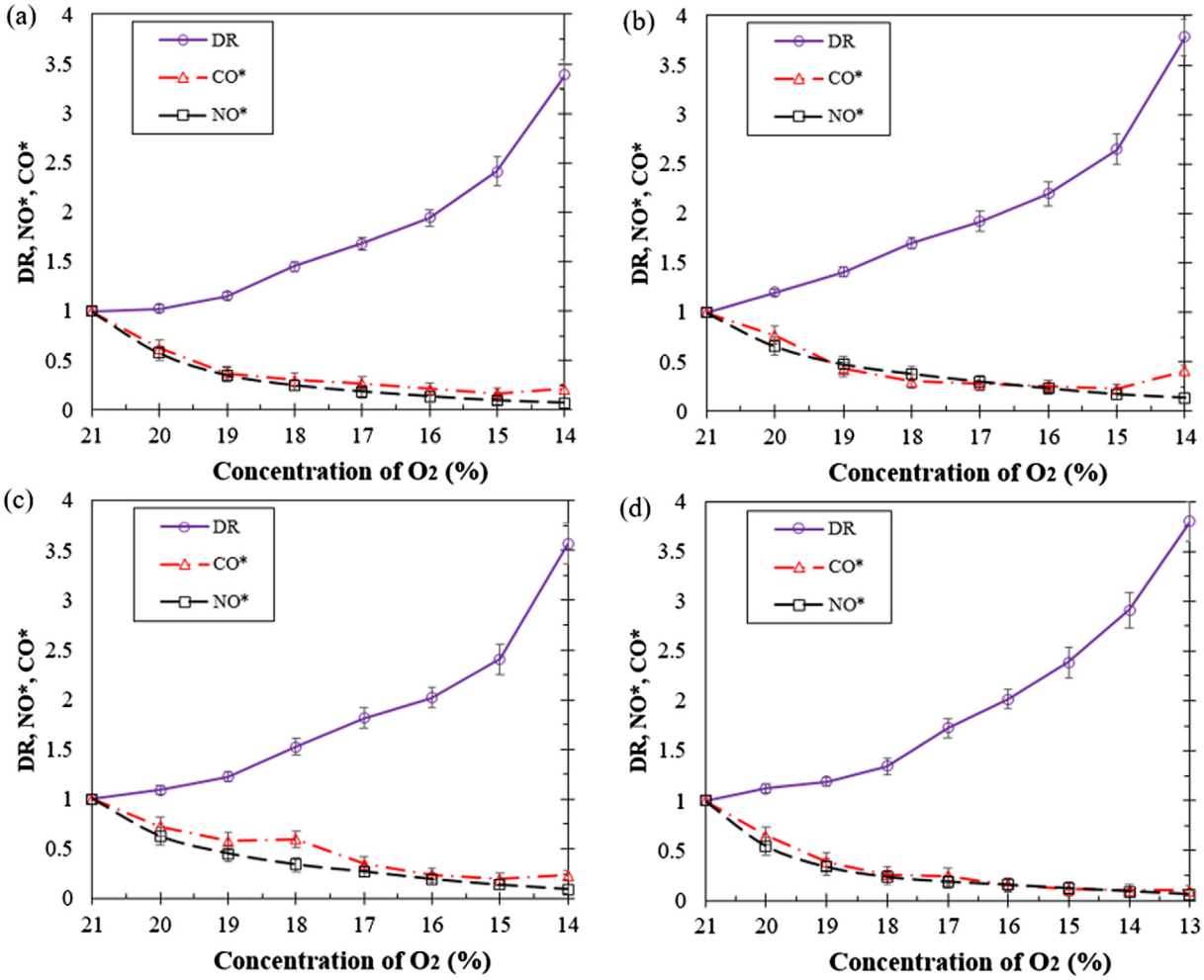

Fig. 13. Normalized NO (or NO*) and CO (or CO*) and DR (area-based) for (a) propane, (b) methane, (c) 20% HEM and (d) 40% HEM flame at different O_2 concentrations using N_2 as flow diluent.

fluctuation reduced from ~20–25% to less than 2% of mean intensity when CDC mode was achieved. Flame expansion with respect to their initial volume (in air combustion) provided a better understanding on the role of chemical composition of different fuels under CDC. The results showed a power law growth behavior of different flames for both the diluents. Normalized flame lift-off height revealed the different combustion behavior of flames. The lift-off height for CO_2 diluted flow field was observed to be higher than the N_2 diluted flow field. Higher heat capacity value of CO_2 promoted greater reduction of flame speed that subsequently caused in higher flame lift-off to occur. The pollutants emission (normalized NO and CO concentrations) showed a significant reduction when the flames approached distributed combustion mode. The use of CO_2 diluent provided an increase in CO concentration at intermediate O_2 levels primarily due to the dissociation of CO_2 to CO at high temperatures. Such observation of increased CO level was additionally supported by simplified chemical analysis in Chemkin-Pro® coupled with GRI 3.0, which manifested good agreement with the CO levels observed during experiments. The results on flame volumetric expansion with reduced pollutants emission help in the design and development of next generation ultra-low emission gas turbine combustors.

Declaration of Competing Interest

The authors declare that they have no known competing financial interests or personal relationships that could have appeared to influence the work reported in this paper.

Acknowledgments

The authors gratefully acknowledge the support provided by the Office of Naval Research (ONR) for this research. The authors also thank Dr. Serhat Karyeyen and Mr. Joseph S. Feser for their assistance during experiments for the results presented here.

References

[1] Steinberg M. Fossil fuel decarbonization technology for mitigating global warming. Int J Hydrogen Energy 1999;24:771–7. https://doi.org/10.1016/S0360-3199(98)0012-1.
[2] Bahr DW. Aircraft Engines NO Emissions – Abatement Progress and Prospects. Proceedings of Tenth International Symposium on Air-breathing Engines, Nottingham, England, September 1-6, 1991.
[3] Rahm S, Goldmeer J, Molière M, Eranki A. Addressing gas turbine fuel flexibility. GE report GER4601. Available at the website: http://www.gepower.com/prod_serv/products/tech_docs/en/downloads/GER4601.pdf, [accessed 12.12.09], June 09.
[4] Mosier SA, Pierce RM. Advanced Combustor Systems for Stationary Gas Turbine Engines, Phase I. Review and Preliminary Evaluation, Final Report, U.S. Environmental Protection Agency, Contract 68-02-2136, FR-11405, 1980; Vol. 1.
[5] Correa SM. Lean premixed combustion for gas-turbines: review and acquired research. In: Ruiz R, editor. Energy-sources technology conference and exhibition, Fossil Fuel Combustion, Houston, TX: ASME January 20–23, 1991; 33:1–9.
[6] Lammel O, Schutz H, Schmitz G, Luckerath R, Stohr M, Noll B, et al. FLOX® combustion at high power density and high flame temperature. J Eng Gas Turbine Power, 132. 2010. https://doi.org/10.1115/1.4001825.
[7] Zornek T, Monz T, Aigner M. Performance analysis of the micro gas turbine Turbec T100 with a new FLOX-combustion system for low calorific fuels. Appl Energy 2015;159:276–84. https://doi.org/10.1016/j.apenergy.2015.08.075.
[8] Cavaliere A, De Joannon M. Mild combustion. Prog Energy Combust Sci 2004;30(4):329–66. https://doi.org/10.1016/j.pecs.2004.02.003.
[9] Sabia P, Sorrentino G, Bozza P, Ceriello G, Ragucci R, De Joannon M. Fuel and thermal load flexibility of a MILD burner. Proc Comb Inst. 2019;37(4):4547–54. https://doi.org/10.1016/j.proci.2018.09.003.
[10] Khalil AEE, Gupta AK. Swirling distributed combustion for clean energy conversion in gas turbine applications. Appl Energy 2011;88(11):3685–93. https://doi.org/10.1016/j.apenergy.2011.03.048.
[11] Khalil AEE, Gupta AK, Bryden MK, Lee SC. Mixture preparation effects on distributed combustion for gas turbine applications. J Energy Resour Technol 2012;134(3):032201https://doi.org/10.1115/1.4006481.
[12] Khalil AEE, Gupta AK. Velocity and turbulence effect on high intensity distributed combustion. Appl Energy 2014;125:1–9. https://doi.org/10.1016/j.apenergy.2013.11.078.
[13] Tsuji H, Gupta AK, Hasegawa T, Katsuki M, Kishimoto K, Morita M. High temperature air combustion: from energy conservation to pollution reduction. Boca Raton (Florida): CRC Press; 2003.
[14] Arghode VK, Gupta AK, Bryden KM. High intensity colorless distributed combustion for ultra-low emissions and enhanced performance. Appl Energy 2012;92:822–30. https://doi.org/10.1016/j.apenergy.2011.08.039.
[15] Khalil AEE, Gupta AK. Acoustic and heat release signatures for swirl assisted distributed combustion. Appl Energy 2017;193:125–38. https://doi.org/10.1016/j.apenergy.2017.02.030.
[16] Correa SM. A review of NOx formation under gas-turbine combustion conditions. Combust Sci Technol 1992;87:329–62. https://doi.org/10.1080/00102209208947221.
[17] Duwig C, Li B, Li ZS, Aldén M. High resolution imaging of flameless and distributed turbulent combustion. Combust Flame 2012;159(1):306–16. https://doi.org/10.1016/j.combustflame.2011.06.018.
[18] Dally BB, Karpetis AN, Barlow RS. Structure of turbulent non-premixed jet flames in a diluted hot co-flow. Proc Combust Inst 2002;29(1):1147–54. https://doi.org/10.1016/S1540-7489(02)80145-6.
[19] Anand MS, Pope SB. Flamelet and distributed combustion in premixed turbulent flame. Twentieth Symposium (International) on Combustion, Ann Arbor, Michigan, August 12-17, 1984/The Combustion Institute 1985; 20(1):403-410. doi: 10.1016/S0082-0784(85)80527-0.
[20] Arghode VK, Gupta AK. Investigation of forward flow distributed combustion for gas turbine application. J Appl Energy 2010;88(1):29–40. https://doi.org/10.1016/j.apenergy.2010.04.030.
[21] Arghode VK, Gupta AK. Investigation of reverse flow distributed combustion for gas turbine application. Appl Energy 2011;88(4):1096–104. https://doi.org/10.1016/j.apenergy.2010.10.039.
[22] Arghode VK, Gupta AK. Hydrogen addition effects on methane-air colorless distributed combustion flames. Int J Hydrogen Energy 2011;36(10):6292–302. https://doi.org/10.1016/j.ijhydene.2011.02.028.
[23] Arghode VK, Gupta AK. Development of high intensity CDC combustor for gas turbine engines. Appl Energy 2011;88(3):963–73. https://doi.org/10.1016/j.apenergy.2010.07.038.
[24] Khalil AEE, Gupta AK. Impact of pressure on high intensity colorless distributed combustion. Fuel 2015;143:334–42. https://doi.org/10.1016/j.fuel.2014.11.061.
[25] Khalil AEE, Gupta AK. Distributed swirl combustion for gas turbine application. Appl Energy 2011;88(12):4898–907. https://doi.org/10.1016/j.apenergy.2011.06.051.
[26] Arghode VK, Khalil AEE, Gupta AK. Fuel dilution and liquid fuel operational effects on ultra-high thermal intensity distributed combustor. Appl Energy 2012;95:132–8. https://doi.org/10.1016/j.apenergy.2012.02.020.
[27] Sorrentino G, Sabia P, de Joannon M, Bozza P, Ragucci R. Influence of preheating and thermal power on cyclonic burner characteristics under mild combustion. Fuel 2018;233:207–14. https://doi.org/10.1016/j.fuel.2018.06.049.
[28] Schütz H, Lammel O, Schmitz G, Rödiger T, Aigner M. EZEE®: A high power density modulating FLOX® combustor. In: ASME Turbo Expo 2012: Turbine Technical Conference and Exposition, Copenhagen, Denmark, ASME 2012, GT2012-68997:701-712. doi: 10.1115/GT2012-68997.
[29] Khalil AEE, Gupta AK. Swirling flowfield for colorless distributed combustion. Appl Energy 113 2014;208(218). https://doi.org/10.1016/j.apenergy.2013.07.029.
[30] Khalil AEE, Gupta AK. Impact of internal entrainment on high intensity distributed combustion. Appl Energy 2015;156:241–50. https://doi.org/10.1016/j.apenergy.2015.07.044.
[31] Khalil AEE, Gupta AK. On the flame–flow interaction under distributed combustion conditions. Fuel 2016;182:17–26. https://doi.org/10.1016/j.fuel.2016.05.071.
[32] Khalil AEE, Gupta AK. The role of CO2 on oxy-colorless distributed combustion. Appl Energy 2017;188:466–74. https://doi.org/10.1016/j.apenergy.2016.12.048.
[33] Arghode VK, Gupta AK. Effect of flow field for colorless distributed combustion (CDC) for gas turbine combustion. Appl Energy 2010;87(5):1631–40. https://doi.org/10.1016/j.apenergy.2009.09.032.
[34] Feser JS, Bassioni G, Gupta AK. Effect of naphthalene addition to ethanol in distributed combustion. Appl Energy 2018;216:1–7. https://doi.org/10.1016/j.apenergy.2018.02.090.
[35] Karyeyen S, Feser JS, Gupta AK. Hydrogen concentration effects on swirl-stabilized oxy-colorless distributed combustion. Fuel 2019;253:772–80. https://doi.org/10.1016/j.fuel.2019.05.008.
[36] Khalil AEE, Brooks JM, Gupta AK. Impact of confinement on flowfield of swirl flow burners. Fuel 2016;184:1–9. https://doi.org/10.1016/j.fuel.2016.06.098.
[37] Altay HM, Speth RL, Hudgins DE, Ghoniem AF. The impact of equivalence ratio oscillations on combustion dynamics in a backward-facing step combustor. Combust Flame 2009;156(11):2106–16. https://doi.org/10.1016/j.combustflame.2009.07.024.
[38] Lieuwen T. Modeling premixed combustion-acoustic wave interactions: a review. J Propul Power 2003;19(5):765–81. https://doi.org/10.2514/2.6193.
[39] Ayoola BO, Balachandran R, Frank JH, Mastorakos E, Kaminski CF. Spatially resolved heat release rate measurements in turbulent premixed flames. Combust Flame 2006;144(1–2):1–16. https://doi.org/10.1016/j.combustflame.2005.06.005.
[40] He L, Guo Q, Gong Y, Wang F, Yu G. Investigation of OH* chemiluminescence and heat release in laminar methane–oxygen co-flow diffusion flames. Combust Flame 2019;201:12–22. https://doi.org/10.1016/j.combustflame.2018.12.009.
[41] Khalil AEE, Gupta AK. Thermal field investigation under distributed combustion conditions. J Appl Energy 2015;160:477–88. https://doi.org/10.1016/j.apenergy.2015.09.058.
[42] Giassi D, Cao S, Bennett BAV, Stocker DP, Takahashi F, Smooke MD, et al. Analysis of CH* concentration and flame heat release rate in laminar coflow diffusion flames under microgravity and normal gravity. Combust Flame 2016;167:198–206.

[43] Sweeney M, Hochgreb S. Autonomous extraction of optimal flame fronts in OH planar laser-induced fluorescence images. Appl Opt 2009;48(19):3866–77. https://doi.org/10.1364/AO.48.003866.
[44] Nobuyuki O. A threshold selection method from gray-level histograms. IEEE Trans Syst Man Cybern 1979;9(1):62–6. https://doi.org/10.1109/TSMC.1979.4310076.
[45] Roy R. Experimental Investigation of the Dynamics and Blowoff Characteristics of Bluff-body Stabilized 2D, V-Shaped Turbulent Premixed Flames with Different Gaseous Hydrocarbon Fuels. MS Thesis, University of Connecticut 2019. https://opencommons.uconn.edu/gs_theses/1318.
[46] Malm H, Sparr G, Hult J, Kaminski CF. Nonlinear diffusion filtering of images obtained by planar-laser-induced fluorescence spectroscopy. J Opt Soc Am A 2000;17(12):2148–56. https://doi.org/10.1364/JOSAA.17.002148.
[47] Perona P, Malik J. Scale-space and edge detection using anisotropic diffusion. IEEE Trans Pattern Anal Mach Intell 1990;12(7):629–39. https://doi.org/10.1109/34.56205.
[48] Liu X, Tanaka M, Okutomi M. Single-image noise level estimation for blind denoising. IEEE Trans Image Process 2013;22(12):5226–37. https://doi.org/10.1109/TIP.2013.2283400.
[49] Alternatives to Traditional Transportation Fuels: An Overview. DOE/EIA-0585/OF. Energy Information Administration. U.S. Department of Energy. Washington, DC. June 1994.
[50] Schefer RW, Wicksall DM, Agrawal AK. Combustion of hydrogen-enriched methane in a lean premixed swirl-stabilized burner. Proceedings of the 29th symposium (international) on combustion 2002; 29(1):843–51. doi: 10.1016/S1540-7489(02)80108-0.
[51] Lantz A, Collin R, Aldén M, Lindholm A, Larfeldt J, Lörstad D. Investigation of hydrogen enriched natural gas flames in a SGT-700/800 burner using OH PLIF and chemiluminescence imaging. ASME J Eng Gas Turbines Power 2014;137(3). https://doi.org/10.1115/1.4028462. 031505-031505-8.
[52] Khalil AEE, Gupta AK. Fuel property effect on distributed combustion. Fuel 2016;171:116–24. https://doi.org/10.1016/j.fuel.2015.12.068.
[53] Karyeyen S, Feser JS, Gupta AK. Swirl assisted distributed combustion behavior using hydrogen-rich gaseous fuels. Appl Energy 2019;251:113354. https://doi.org/10.1016/j.apenergy.2019.113354.
[54] Natarajan J, Lieuwen T, Seitzman J. Laminar flame speeds of H2/CO mixtures: effect of CO2 dilution, preheat temperature, and pressure. Combust Flame 2007;151(1–2):104–19. https://doi.org/10.1016/j.combustflame.2007.05.003.
[55] Durbin MD, Vangsness MD, Ballal DR, Katta VR. Study of flame stability in a step swirl combustor. ASME J Eng Gas Turbines Power 1996;118(2):308–15. https://doi.org/10.1115/1.2816592.
[56] Rortveit GJ, Hustad JE, Li SC, Williams FA. Effects of diluents on NOx formation in hydrogen counterflow flames. Combust Flame 2002;130(1–2):48–61. https://doi.org/10.1016/S0010-2180(02)00362-0.
[57] Smith GP, Golden DM, Frenklach M, Moriarty NW, Eiteneer B, Goldenburg M, et al. GRI 3.0 Mechanism, http://www.me.berkeley.edu/gri_mech/.
[58] Coltrin ME, Dandy DS. Analysis of diamond growth in subatmospheric dc plasma-gun reactor. J Appl Phys 1998;74:5803. https://doi.org/10.1063/1.354201.
[59] Leung KM, Lindstedt RP. Detailed kinetic modeling of C1–C3 alkane diffusion flames. Combust Flame 1995;102:129–60. https://doi.org/10.1016/0010-2180(94)00254-PGet.